Supporting Information

S1 Appendix: Computational Details and Explicit Equations Used

In this section, we first present the governing equations for the flow in our thermal convection loop experiment. A spatial and temporal discretization of the governing equations is then necessary so that they may be solved numerically. After discretization, we must specify the boundary conditions. With the mesh and boundary conditions in place, we can then simulate the flow with a computational fluid dynamics solver.

We now discuss the equations, mesh, boundary conditions, and solver in more detail. With these considerations, we present our simulations of the thermosyphon. For a complete derivation of the equations used, see [35].

We consider the incompressible Navier-Stokes equations with the Boussinesq approximation to model the flow of water inside a thermal convection loop. Here we present the main equations that are solved numerically, noting the assumptions that are necessary in their derivation. In standard notation, for u, v, w the velocity in the x, y, z direction, respectively, the continuity equation for an incompressible fluid is

$$\frac{\partial u}{\partial x} + \frac{\partial v}{\partial y} + \frac{\partial w}{\partial z} = 0. \tag{S1}$$

The momentum equations, in tensor notation with bars representing averaged quantities (long timesteps are used, requiring integration), are

$$\rho_{\text{ref}} \left(\frac{\partial \bar{u}_i}{\partial t} + \frac{\partial}{\partial x_j} \left(\bar{u}_j \bar{u}_i \right) \right) = -\frac{\partial \bar{p}}{\partial x_i} + \mu \frac{\partial \bar{u}_i}{\partial x_j^2} + \rho_{\text{ref}} \left(1 - \beta(T - T_{\text{ref}}) \right) g_i \tag{S2}$$

for ρ_{ref} the reference density with the Boussinesq approximation included, p the pressure, μ the viscosity, and g_i gravity in the i-direction. Note that $g_i = 0$ for $i \in \{x, y\}$ since gravity is assumed to be the z direction. Since the model is incompressible, of course our energy equation includes only temperature, and is given by

$$\frac{\partial T}{\partial t} + \frac{\partial}{\partial x_j} \left(\rho_{\text{ref}} T \bar{u}_j \right) - \frac{\partial^2 \alpha T}{\partial x_j \partial x_i} = -\frac{\partial q_k^*}{\partial x_k} - \frac{\partial \bar{q}_k}{\partial x_k} \tag{S3}$$

for T the temperature and q the flux (where $q = \bar{q} + q^*$ is the averaging notation).

The PISO (Pressure-Implicit with Splitting of Operators) algorithm derives from the work of [23], and is complementary to the SIMPLE (Semi-Implicit Method for Pressure-Linked Equations) [36] iterative method. The main difference of the PISO and SIMPLE algorithms is that in the PISO, no under-relaxation is applied and the momentum corrector step is performed more than once [37]. They sum up the algorithm in nine steps:

- Set the boundary conditions.

- Solve the discretized momentum equation to compute an intermediate velocity field.

- Compute the mass fluxes at the cell faces.

- Solve the pressure equation.

- Correct the mass fluxes at the cell faces.

- Correct the velocity with respect to the new pressure field.

- Update the boundary conditions.

- Repeat from step #3 for the prescribed number of times.

- Repeat (with increased time step).

The solver itself has 647 dependencies, of which I present only a fraction. The main code is straight forward, relying on include statements to load the libraries and equations to be solved.

```
#include "fvCFD.H"
#include "singlePhaseTransportModel.H"
#include "RASModel.H" // AJR edited header 2013-10-14
#include "radiationModel.H" // (model loaded but not used)
#include "fvIOoptionList.H" // (loaded, but also not used)
#include "pimpleControl.H"
```

The main function is then

```
int main(int argc, char *argv[])
{
    #include "setRootCase.H"
    #include "createTime.H"
    #include "createMesh.H"
    #include "readGravitationalAcceleration.H"
    #include "createFields.H"
    #include "createIncompressibleRadiationModel.H"
    #include "createFvOptions.H"
    #include "initContinuityErrs.H"
    #include "readTimeControls.H"
    #include "CourantNo.H"
    #include "setInitialDeltaT.H"
    pimpleControl pimple(mesh);
```

We then enter the main loop. This is computed for each time step, prescribed before the solver is applied. Note that the capacity is available for adaptive time steps, choosing to keep the Courant number below some threshold, but I do not use this. For the distributed ensemble of model runs, it is important that each model complete in nearly the same time, so that the analysis is not waiting on one model and therefore under-utilizing the available resources.

```
    while (runTime.loop())
    {
        #include "readTimeControls.H"
        #include "CourantNo.H"
        #include "setDeltaT.H"
        while (pimple.loop())
        {
            #include "UEqn.H"
            #include "TEqn.H"
            while (pimple.correct())
            {
                #include "pEqn.H"
            }
        }
        if (pimple.turbCorr())
        {
            turbulence->correct();
        }
```

Opening up the equation for U we see that Equation

```
    // Solve the momentum equation
    fvVectorMatrix UEqn
    (
        fvm::ddt(U)
      + fvm::div(phi, U)
      + turbulence->divDevReff(U)
      ==
        fvOptions(U)
```

```
    );
    UEqn.relax();
    fvOptions.constrain(UEqn);
    if (pimple.momentumPredictor())
    {
        solve
        (
            UEqn
         ==
            fvc::reconstruct
            (
                (
                    - ghf*fvc::snGrad(rhok)
                    - fvc::snGrad(p_rgh)
                )*mesh.magSf()
            )
        );
        fvOptions.correct(U);
    }
```

Solving for T is

```
{
    // with our laminar model, alphat = 0
    alphat = turbulence->nut()/Prt;
    alphat.correctBoundaryConditions();
    volScalarField alphaEff("alphaEff", turbulence->nu()/Pr + alphat);
    fvScalarMatrix TEqn
    (
        fvm::ddt(T)
      + fvm::div(phi, T)
      - fvm::laplacian(alphaEff, T)
     ==
        radiation->ST(rhoCpRef, T)
      + fvOptions(T)
    );
    TEqn.relax();
    fvOptions.constrain(TEqn);
    TEqn.solve();
    radiation->correct();
    fvOptions.correct(T);
    rhok = 1.0 - beta*(T - TRef); // Boussinesq approximation
}
```

Finally, we solve for the pressure p in "pEqn.H":

```
{
    volScalarField rAU("rAU", 1.0/UEqn.A());
    surfaceScalarField rAUf("Dp", fvc::interpolate(rAU));
    volVectorField HbyA("HbyA", U);
    HbyA = rAU*UEqn.H();
    surfaceScalarField phig(-rAUf*ghf*fvc::snGrad(rhok)*mesh.magSf());
    surfaceScalarField phiHbyA
    (
        "phiHbyA",
        (fvc::interpolate(HbyA) & mesh.Sf())
      + fvc::ddtPhiCorr(rAU, U, phi)
      + phig
    );
    while (pimple.correctNonOrthogonal())
    {
        fvScalarMatrix p_rghEqn
        (
            fvm::laplacian(rAUf, p_rgh) == fvc::div(phiHbyA)
        );
        p_rghEqn.setReference(pRefCell, getRefCellValue(p_rgh, pRefCell));
        p_rghEqn.solve(mesh.solver(p_rgh.select(pimple.finalInnerIter())));
        if (pimple.finalNonOrthogonalIter())
        {
            // Calculate the conservative fluxes
            phi = phiHbyA - p_rghEqn.flux();
            // Explicitly relax pressure for momentum corrector
            p_rgh.relax();
            // Correct the momentum source with the pressure gradient flux
            // calculated from the relaxed pressure
            U = HbyA + rAU*fvc::reconstruct((phig - p_rghEqn.flux())/rAUf);
            U.correctBoundaryConditions();
        }
```

```
            }
        }
        #include "continuityErrs.H"
        p = p_rgh + rhok*gh;
        if (p_rgh.needReference())
        {
            p += dimensionedScalar
            (
                "p",
                p.dimensions(),
                pRefValue - getRefCellValue(p, pRefCell)
            );
            p_rgh = p - rhok*gh;
        }
    }
```

The final operation being the conversion of pressure to hydrostatic pressure,

$$p_{\text{rgh}} = p - \rho_k g_h.$$

This "pEqn.H" is then re-run until convergence is achieved, and the PISO loop begins again.

We verify convergence of the solution in a steady flow state regime in Fig S1.
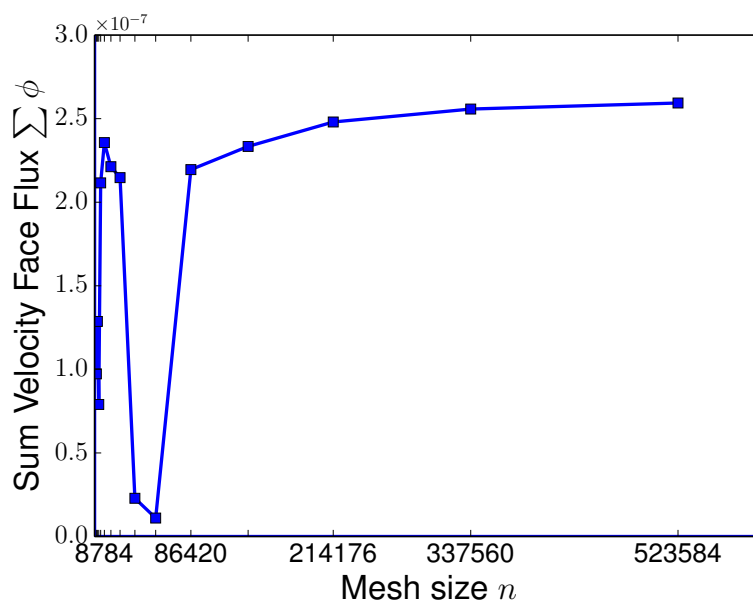

Figure S1. With a fixed choice of solver, boundary conditions, and initial conditions that lead to a stable convective state, we present the long-term behavior of the velocity face flux at the top slice for different meshes. The face flux is reported as the average for the last 20 times saves for which the velocity flux is summed across a slice perpendicular to the loop, here we show the top slice. We choose a fixed time step of 0.005 for each simulation, and run the solver for 60 hours on 8 cores. The computational limit of mesh creation was a memory limit at 818280 cells, so we present results for meshes starting at 1600 cells and cells decreasing in size by a factor of 1.25 in both y and z up to a mesh of 523584 cells. For meshes with more than 80,000 cells we see that the solutions are very similar. The smaller meshes generate increasing unstable flow behavior, leading to oscillations of flux and then flow reversals for the smallest meshes of size 2500 and 1600 cells.

S2 Appendix: The Ehrhard and Müller Equations

Following the derivation by Harris [8], itself a representation of the derivation of Gorman [13] and namesakes Ehrhard and Müller [14], we derive the equations governing a closed loop thermosyphon.

Similar to the derivation of the governing equations of computational fluid dynamics, we start with a small but finite volume inside the loop. Here, however, the volume is described by $\pi r^2 R \mathrm{d}\phi$ for r the interior loop size (such that πr^2 is the area of a slice) and $R \mathrm{d}\phi$ the arc length (width) of the slice. Newton's second law states that momentum is conserved, such that the sum of the forces acting upon our finite volume is equal to the change in momentum of this volume. Therefore we have the basic starting point for forces $\sum F$ and velocity u as

$$\sum F = \rho \pi r^2 R \mathrm{d}\phi \frac{\mathrm{d}u}{\mathrm{d}t}. \tag{S4}$$

The sum of the forces is $\sum F = F_{\{p,f,g\}}$ for net pressure, fluid shear, and gravity, respectively. We write these as

$$F_p = -\pi r^2 \mathrm{d}\phi \frac{\partial p}{\partial \phi} \tag{S5}$$

$$F_w = -\rho \pi r^2 \mathrm{d}\phi f_w \tag{S6}$$

$$F_g = -\rho \pi r^2 \mathrm{d}\phi g \sin(\phi) \tag{S7}$$

where $\partial p / \partial \phi$ is the pressure gradient, f_w is the wall friction force, and $g \sin(\phi)$ is the vertical component of gravity acting on the volume.

We now introduce the Boussinesq approximation which states that both variations in fluid density are linear in temperature T and density variation is insignificant except when multiplied by gravity. The consideration manifests as

$$\rho = \rho(T) \simeq \rho_{\mathrm{ref}}(1 - \beta(T - T_{\mathrm{ref}})$$

where ρ_0 is the reference density and T_{ref} is the reference temperature, and β is the thermal expansion coefficient. The second consideration of the Boussinesq approximation allows us to replace ρ with this ρ_{ref} in all terms except for F_g. We now write momentum equation as

$$-\pi r^2 \mathrm{d}\phi \frac{\partial p}{\partial \phi} - \rho_{\mathrm{ref}} \phi r^2 R \mathrm{d}\phi f_w - \rho_{\mathrm{ref}}(1 - \rho(T - T_{\mathrm{ref}})) \pi r^2 R \mathrm{d}\phi g \sin(\phi) = \rho_{\mathrm{ref}} \pi r^2 R \mathrm{d}\phi \frac{\mathrm{d}u}{\mathrm{d}t}. \tag{S8}$$

Canceling the common πr^2, dividing by R, and pulling out $\mathrm{d}\phi$ on the LHS we have

$$-\mathrm{d}\phi \left(\frac{\partial p}{\partial \phi} \frac{1}{R} - \rho_{\mathrm{ref}} f_w - \rho_{\mathrm{ref}}(1 - \rho(T - T_{\mathrm{ref}})) g \sin(\phi) \right) = \rho_{\mathrm{ref}} \mathrm{d}\phi \frac{\mathrm{d}u}{\mathrm{d}t}. \tag{S9}$$

We integrate this equation over ϕ to eliminate many of the terms, specifically we have

$$\int_0^{2\pi} -\mathrm{d}\phi \frac{\partial p}{\partial \phi} \frac{1}{R} \to 0$$

$$\int_0^{2\pi} -\mathrm{d}\phi \rho_{\mathrm{ref}} g \sin(\phi) \to 0$$

$$\int_0^{2\pi} -\mathrm{d}\phi \rho_{\mathrm{ref}} \beta T_{\mathrm{ref}} g \sin(\phi) \to 0.$$

Since u (and hence $\frac{du}{d\phi}$) and f_w do not depend on ϕ, we can pull these outside an integral over ϕ and therefore the momentum equation is now

$$2\pi f_w \rho_0 + \int_0^{2\pi} d\phi \rho_{\text{ref}} \beta T g \sin(\phi) = 2\pi \frac{du}{d\phi} \rho_{\text{ref}}.$$

Diving out 2π and pull constants out of the integral we have our final form of the momentum equation

$$f_w \rho_{\text{ref}} + \frac{\rho_{\text{ref}} \beta g}{2\pi} \int_0^{2\pi} d\phi T \sin(\phi) = \frac{du}{d\phi} \rho_{\text{ref}}. \tag{S10}$$

Now considering the conservation of energy within the thermosyphon, the energy change within a finite volume must be balanced by transfer within the thermosyphon and to the walls. The internal energy change is given by

$$\rho_{\text{ref}} \pi r^2 R d\phi \left(\frac{\partial T}{\partial t} + \frac{u}{R} \frac{\partial T}{\partial \phi} \right) \tag{S11}$$

which must equal the energy transfer through the wall, which is, for T_w the wall temperature:

$$\dot{q} = -\pi r^2 R d\phi h_w (T - T_w). \tag{S12}$$

Combining Equations S11 and S12 (and canceling terms) we have the energy equation:

$$\left(\frac{\partial T}{\partial t} + \frac{u}{R} \frac{\partial T}{\partial \phi} \right) = \frac{-h_w}{\rho_{\text{ref}} c_p} (T - T_w). \tag{S13}$$

The f_w which we have yet to define and h_w are fluid-wall coefficients and can be described by [14]:

$$h_w = h_{w_0} (1 + Kh(|x_1|))$$

$$f_w = \frac{1}{2} \rho_{\text{ref}} f_{w_0} u.$$

We have introduced an additional function h to describe the behavior of the dimensionless velocity $x_1 \alpha u$. This function is defined piece-wise as

$$h(x) = \begin{cases} x^{1/3} & \text{when } x \geq 1 \\ p(x) & \text{when } x < 1 \end{cases} \tag{S14}$$

where $p(x)$ can be defined as $p(x) = \left(44x^2 - 55x^3 + 20x^4 \right)/9$ such that p is analytic at 0 [8].

Taking the lowest modes of a Fourier expansion for T for an approximate solution, we consider:

$$T(\phi, t) = C_0(t) + S(t) \sin(\phi) + C(t) \cos(\phi). \tag{S15}$$

By substituting this form into Equations S10 and S13 and integrating, we obtain a system of three equations for our solution. We then follow the particular nondimensionalization choice of Harris *et al.*such that we obtain the following ODE system, which we refer to as the Ehrhard-Müller equations:

$$\frac{dx_1}{dt'} = \alpha(x_2 - x_1), \tag{S16}$$

$$\frac{dx_2}{dt'} = \beta x_1 - x_2(1 + Kh(|x_1|)) - x_1 x_3, \tag{S17}$$

$$\frac{dx_3}{dt'} = x_1 x_2 - x_3(1 + Kh(|x_1|)). \tag{S18}$$

The nondimensionalization is given by the change of variables

$$t' = \frac{h_{w_0}}{\rho_{\text{ref}}c_p}t, \tag{S19}$$

$$x_1 = \frac{\rho_{\text{ref}}c_p}{Rh_{w_0}}u, \tag{S20}$$

$$x_2 = \frac{1}{2}\frac{\rho_{\text{ref}}c_p\beta g}{Rh_{w_0}f_{w_0}}\Delta T_{3-9}, \tag{S21}$$

$$x_3 = \frac{1}{2}\frac{\rho_{\text{ref}}c_p\beta g}{Rh_{w_0}f_{w_0}}\left(\frac{4}{\pi}\Delta T_w - \Delta T_{6-12}\right) \tag{S22}$$

and

$$\alpha = \frac{1}{2}Rc_p f_{w_0}/h_{w_0}, \tag{S23}$$

$$\gamma = \frac{2}{\pi}\frac{\rho_{\text{ref}}c_p\beta g}{Rh_{w_0}f_{w_0}}\Delta T_w. \tag{S24}$$

Through careful consideration of these non-dimensional variable transformations we verify that x_1 is representative of the mean fluid velocity, x_2 of the temperature difference between the 3 and 9 o'clock positions on the thermosyphon, and x_3 the deviation from the vertical temperature profile in a conduction state [8].

S3 Appendix: Data Assimiliation

The TLM is the model which advances an initial perturbation $\delta\mathbf{x}_i$ at timestep i to a final perturbation $\delta\mathbf{x}_{i+1}$ at timestep $i+1$. The dynamical system we are interested in, Lorenz '63, is given as a system of ODE's:

$$\frac{d\mathbf{x}}{dt} = F(\mathbf{x}).$$

We integrate this system using a numerical scheme of our choice (in the given examples we use a second-order Runge-Kutta method), to obtain a model M discretized in time.

$$\mathbf{x}(t) = M[\mathbf{x}(t_0)].$$

Introducing a small perturbation $\mathbf{y}$, we can approximate our model M applied to $\mathbf{x}(t_0) + \mathbf{y}(t_0)$ with a Taylor series around $\mathbf{x}(t_0)$:

$$M[\mathbf{x}(t_0) + \mathbf{y}(t_0)] = M[\mathbf{x}(t_0)] + \frac{\partial M}{\partial \mathbf{x}}\mathbf{y}(t_0) + O[\mathbf{y}(t_0)^2]$$
$$\approx \mathbf{x}(t) + \frac{\partial M}{\partial \mathbf{x}}\mathbf{y}(t_0).$$

We can then solve for the linear evolution of the small perturbation $\mathbf{y}(t_0)$ as

$$\frac{d\mathbf{y}}{dt} = \mathbf{J}\mathbf{y} \tag{S25}$$

where $\mathbf{J} = \partial F/\partial \mathbf{x}$ is the Jacobian of F. We can solve the above system of linear ordinary differential equations using the same numerical scheme as we did for the nonlinear model.

One problem with solving the system of equations given by Equation S25 is that the Jacobian matrix of discretized code is not necessarily identical to the discretization of the Jacobian operator for the analytic system. This is a problem because we need to have the TLM of our model M, which is the time-space discretization of the solution to $d\mathbf{x}/dt = F(\mathbf{x})$. We can apply our numerical method to the $d\mathbf{x}/dt = F(\mathbf{x})$ to obtain M explicitly, and then take the Jacobian of the result. This method is, however, prohibitively costly, since Runge-Kutta methods are implicit. It is therefore desirable to take the derivative of the numerical scheme directly, and apply this differentiated numerical scheme to the system of equations $F(\mathbf{x})$ to obtain the TLM. A schematic of this scenario is illustrated in Figure S2. To that the derivative of numerical code for implementing the EKF on models larger than 3 dimensions (i.e. global weather models written in Fortan), automatic code differentiation is used [38].

To verify our implementation of the TLM, we propagate a small error in the Lorenz '63 system and plot the difference between that error and the TLM predicted error, for each variable (Figure S3).

With a finite ensemble size, the ensemble method is only an approximation and therefore in practice it often fails to capture the full spread of error. To better capture the model variance, additive and multiplicative inflation factors are used to obtain a good estimate of the error covariance matrix (Data Assimilation Section). The spread of ensemble members in the x_1 variable of the Lorenz model, as distance from the analysis, can be seen in Figure S4.

In computing the error covariance $\mathbf{P}_f$ from the ensemble, we wish to add up the error covariance of each forecast with respect to the mean forecast. But this would underestimate the error covariance, since the forecast we're comparing against is used in the ensemble average (to obtain the mean forecast). Therefore, to compute the error
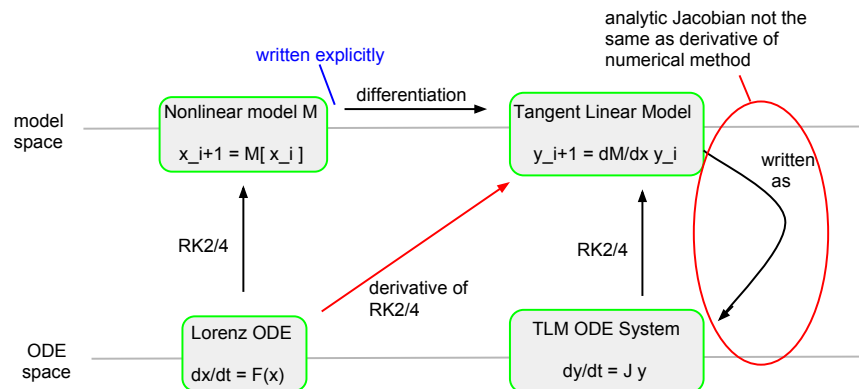
Figure S2. An explanation of how and why the best way to obtain a TLM is with a differentiated numerical scheme. Both the Lorenz ODE and TLM ODE System can be solved by RK2/4, but the analytic Jacobian of TLM that would is not the same as the derivative of the numerical method. In particular, the derivative of the RK2/4 integrator is used to obtain a TLM that most accurately propogates error growth in the Lorenz '63 system.

covariance matrix for each forecast, that forecast itself is excluded from the ensemble average forecast.

We can see the classic spaghetti of the ensemble with this filter implemented on Lorenz 63 in Figure S5.

We denote the forecast within an ensemble filter as the average of the individual ensemble forecasts, and an explanation for this choice is substantiated by Burgers [39]. The general EnKF which we use is most similar to that of Burgers. Many algorithms based on the EnKF have been proposed and include the Ensemble Transform Kalman Filter (ETKF) [31], Ensemble Analysis Filter (EAF) [40], Ensemble Square Root Filter (EnSRF) [41], Local Ensemble Kalman Filter (LEKF) [31], and the Local Ensemble Transform Kalman Filter (LETKF) [32]. A comprehensive overview through 2003 is provided by Evensen [42]. For further details on the most advanced methods, beyond what is provided in the body of the paper, we direct the reader the above references and the derivations provided in [35].
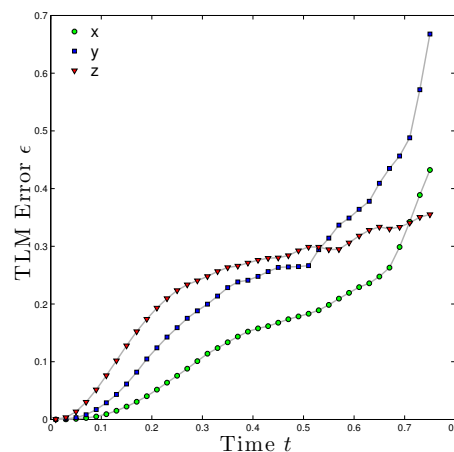
Figure S3. The future error predicted by the TLM is compared to the error growth in Lorenz '63 system for an initial perturbation with standard deviation of 0.1, averaged over 1000 TLM integrations. The ϵ is not the error predicted by the TLM, but rather the error of the TLM in predicting the error growth. We see an intially linear error growth for small time, which is overcome by the nonlinearity of the Lorenz system for longer time.
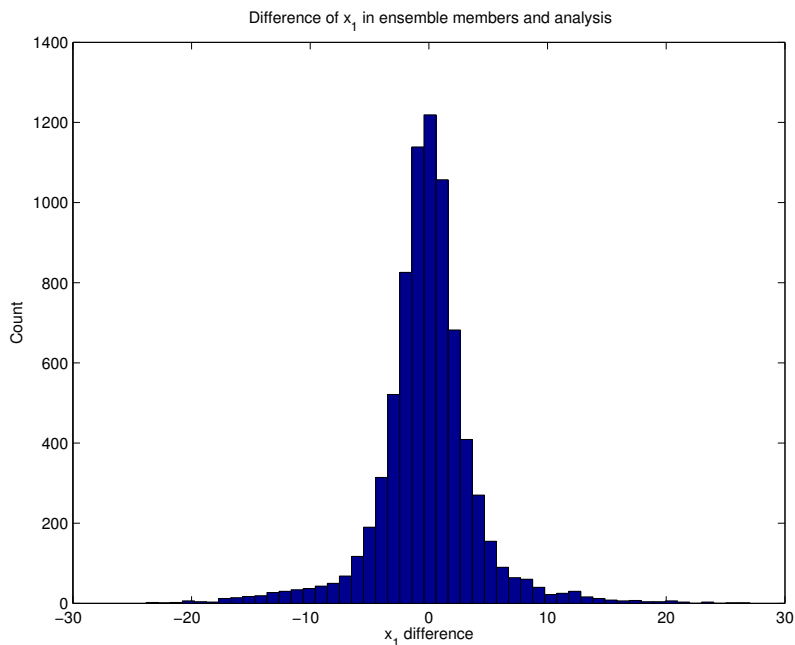

Figure S4. The difference of ensemble forecasts from the analysis is reported for 760 assimilation windows in one model run of length 200, with 10 ensemble members and an assimilation window of length 0.261. This has the same shape of as the difference between ensemble forecasts and the mean of the forecasts (not shown). This spread of ensemble forecasts is what allows us to estimate the error covariance of the forecast model, and appears to be normally distributed.
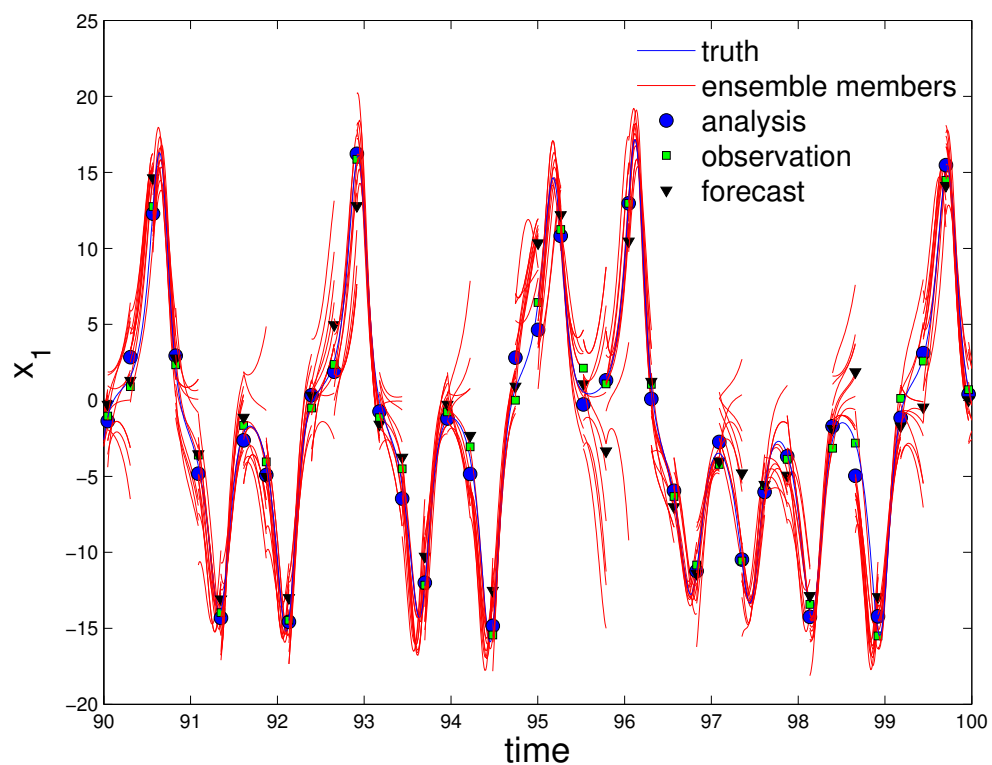
Figure S5. **A sample time-series of the ensembles used in the EnKF.** In all tests, as seen here, 10 ensemble members are used. For this run, 384 assimilation cycles are performed with a window length of 0.26 model time units. We can see that the ensemble member state after assimilation better represents the uncertainty of the analysis state and enables some ensemble members to stay close to the true state.

S4 Appendix: Additional DMD Details

The general algorithm for DMD is provided in the Dynamic Mode Decomposition Section, and here we supply more results of the DMD procedure. The timeseries from which we computed the decomposition is shown in Figure S6.
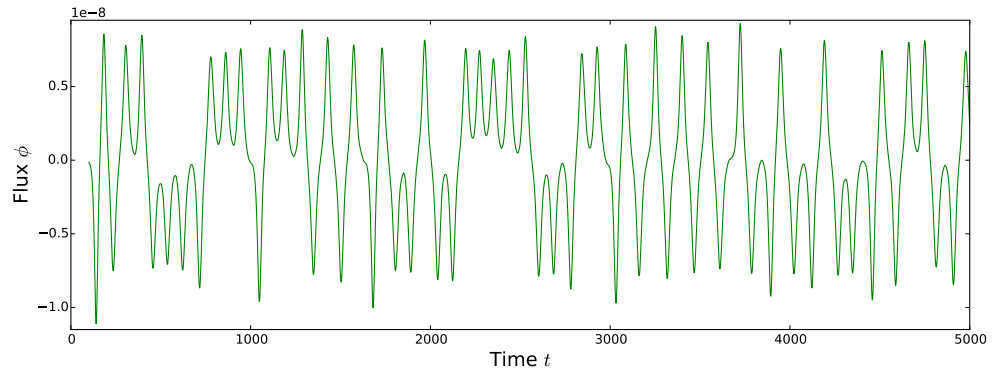

Figure S6. Flux timeseries on which DMD is performed.   We report the flux as the sum of the face flux values on a slice of the loop at the 9 o'clock position. In this flux timeseries we see dynamics visually similar to the x_1 variable of the Lorenz 63 system. Residence time in either flow direction is aperiodic and unstable with the flow speed oscillating within a single direction with growing amplitude until reversing.

The real and imaginary components of the DMD eigenvalues are shown in both un-mapped and mapped form in Figure S7.
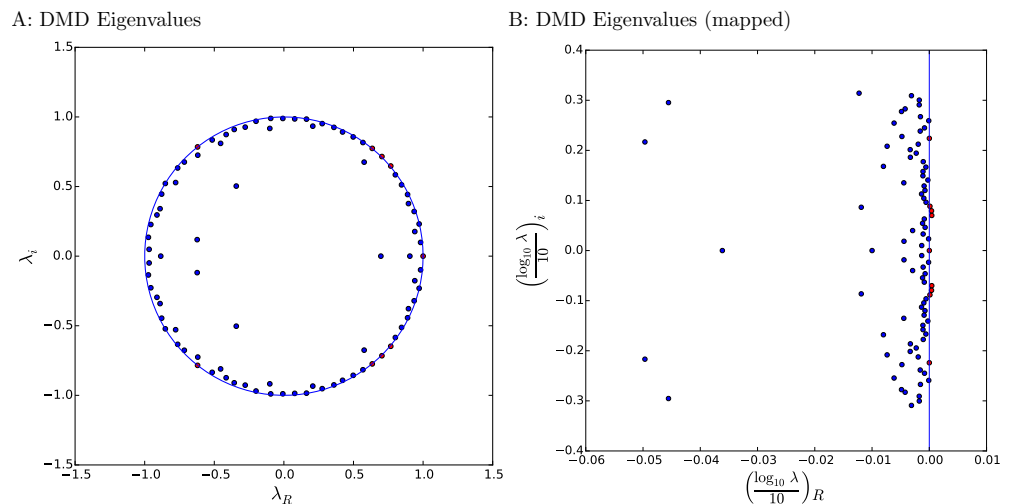

Figure S7. Eigenvalues of DMD Modes presented in both raw and scaled (mapped) form.   In Panel A we see the eigenvalue of each DMD mode on the complex plane, with an inset unit circle. Those eigenvalues with magnitude greater than 1 are shown in red. In Panel B we see the same eigenvalues on the complex plane, transformed by the base 10 logarithm. Again we color in red those eigenvalues with real part greater than 0.

References

1. Hsiang SM, Burke M, Miguel E. Quantifying the Influence of Climate on Human Conflict. Science. 2013;341(6151). Available from: http://www.sciencemag.org/content/341/6151/1235367.abstract.

2. Ginsberg J, Mohebbi MH, Patel RS, Brammer L, Smolinski MS, Brilliant L. Detecting influenza epidemics using search engine query data. Nature. 2008;457(7232):1012–1014.

3. Sornette D, Zhou WX. Predictability of large future changes in major financial indices. International Journal of Forecasting. 2006;22(1):153–168.

4. Asur S, Huberman BA. Predicting the future with social media. In: Web Intelligence and Intelligent Agent Technology (WI-IAT), 2010 IEEE/WIC/ACM International Conference on. vol. 1. IEEE; 2010. p. 492–499.

5. Savely R, Cockrell B, , Pines S. Apollo Experience Report - Onboard Navigational and Alignment Software. Technical Report. 1972;.

6. Bauer P, Thorpe A, Brunet G. The quiet revolution of numerical weather prediction. Nature. 2015;525(7567):47–55.

7. Yang SC, Baker D, Li H, Cordes K, Huff M, Nagpal G, et al. Data Assimilation as Synchronization of Truth and Model: Experiments with the Three-Variable Lorenz System*. Journal of the atmospheric sciences. 2006;63(9):2340–2354.

8. Harris KD, Ridouane EH, Hitt DL, Danforth CM. Predicting flow reversals in chaotic natural convection using data assimilation. arXiv preprint arXiv:11085685. 2011;.

9. Keller JB. Periodic oscillations in a model of thermal convection. J Fluid Mech. 1966;26(3):599–606.

10. Welander P. On the oscillatory instability of a differentially heated fluid loop. International Geophysics Series. 1995;59.

11. Creveling H, PAZ D, Baladi J, Schoenhals R. Stability characteristics of a single-phase free convection loop. Journal of Fluid Mechanics. 1975;67(part 1):65–84.

12. Gorman M, Widmann P. Chaotic flow regimes in a convection loop. Phys Rev Lett. 1984;(52):2241–2244.

13. Gorman M, Widmann P, Robbins K. Nonlinear dynamics of a convection loop: a quantitative comparison of experiment with theory. Physica D. 1986;(19):255–267.

14. Ehrhard P, Müller U. Dynamical behaviour of natural convection in a single-phase loop. Journal of Fluid mechanics. 1990;217:487–518.

15. Yuen P, Bau H. Optimal and adaptive control of chaotic convection. Phys Fluids. 1999;(11):1435–1448.

16. Jiang Y, Shoji M. Spatial and temporal stabilities of flow in a natural circulation loop: influences of thermal boundary condition. J Heat Trans. 2003;(125):612–623.

17. Burroughs E, Coutsias E, Romero L. A reduced-order partial differential equation model for the flow in a thermosyphon. Journal of Fluid Mechanics. 2005;543:203–238.

18. Desrayaud G, Fichera A, Marcoux M. Numerical investigation of natural circulation in a 2D-annular closed-loop thermosyphon. International journal of heat and fluid flow. 2006;27(1):154–166.

19. Ridouane EH, Danforth CM, Hitt DL. A 2-D numerical study of chaotic flow in a natural convection loop. International Journal of Heat and Mass Transfer. 2010;53(1):76–84.

20. Louisos WF, Hitt DL, Danforth CM. Chaotic flow in a 2D natural convection loop with heat flux boundaries. International Journal of Heat and Mass Transfer. 2013;61:565–576.

21. Glenn D. Characterizing weather in a thermosyphon: an atmosphere that hangs on a wall; 2013. Undergraduate Honors Thesis, University of Vermont.

22. Jasak H, Jemcov A, Tukovic Z. OpenFOAM: A C++ library for complex physics simulations. In: International Workshop on Coupled Methods in Numerical Dynamics, IUC, Dubrovnik, Croatia; 2007. p. 1–20.

23. Issa RI. Solution of the implicitly discretised fluid flow equations by operator-splitting. Journal of Computational physics. 1986;62(1):40–65.

24. Lorenc AC. Analysis methods for numerical weather prediction. Quarterly Journal of the Royal Meteorological Society. 1986;112(474):1177–1194.

25. Kalnay E. Atmospheric modeling, data assimilation, and predictability. Cambridge university press; 2003.

26. Danforth CM, Kalnay E, Miyoshi T. Estimating and correcting global weather model error. Monthly weather review. 2007;135(2):281–299.

27. Li H, Kalnay E, Miyoshi T, Danforth CM. Accounting for model errors in ensemble data assimilation. Monthly Weather Review. 2009;137(10):3407–3419.

28. Danforth CM, Kalnay E. Using singular value decomposition to parameterize state-dependent model errors. Journal of the Atmospheric Sciences. 2008;65(4):1467–1478.

29. Bishop CH, Etherton BJ, Majumdar SJ. Adaptive sampling with the ensemble transform Kalman filter. Part I: Theoretical aspects. Monthly weather review. 2001;129(3):420–436.

30. Kalnay E, Li H, Miyoshi T, Yang SC, Ballabrera-Poy J. 4-D-Var or ensemble Kalman filter? Tellus A. 2007;59(5):758–773.

31. Ott E, Hunt BR, Szunyogh I, Zimin AV, Kostelich EJ, Corazza M, et al. A local ensemble Kalman filter for atmospheric data assimilation. Tellus A. 2004;56(5):415–428.

32. Hunt BR, Kostelich EJ, Szunyogh I. Efficient data assimilation for spatiotemporal chaos: A local ensemble transform Kalman filter. Physica D: Nonlinear Phenomena. 2007;230(1):112–126.

33. Tu JH, Rowley CW, Luchtenburg DM, Brunton SL, Kutz JN. On dynamic mode decomposition: theory and applications. arXiv preprint arXiv:13120041. 2013;.

34. Bishop CH, Hodyss D. Adaptive Ensemble Covariance Localization in Ensemble 4D-VAR State Estimation. Monthly Weather Review. 2011 April;139(4):7.

35. Reagan A. Predicting Flow Reversals in a Computational Fluid Dynamics Simulated Thermosyphon using Data Assimilation. arXiv:13122142. 2013;.

36. Patankar SV, Spalding DB. A calculation procedure for heat, mass and momentum transfer in three-dimensional parabolic flows. International Journal of Heat and Mass Transfer. 1972;15(10):1787–1806.

37. Ferziger JH, Perić M. Computational methods for fluid dynamics. vol. 3. Springer Berlin; 1996.

38. Rall LB. Automatic Differentiation: Techniques and Applications (Lecture Notes in Computer Science). Springer; 1981.

39. Burgers G, Jan van Leeuwen P, Evensen G. Analysis scheme in the ensemble Kalman filter. Monthly weather review. 1998;126(6):1719–1724.

40. Anderson MJ. A new method for non-parametric multivariate analysis of variance. Austral Ecology. 2001;26(1):32–46.

41. Tippett MK, Anderson JL, Bishop CH, Hamill TM, Whitaker JS. Ensemble square root filters*. Monthly Weather Review. 2003;131(7):1485–1490.

42. Evensen G. The ensemble Kalman filter: Theoretical formulation and practical implementation. Ocean dynamics. 2003;53(4):343–367.